Interaction of Saturn's magnetosphere and its moons: 3. Time variation of the Enceladus plume

Y.-D. Jia,[1] C. T. Russell,[1] K. K. Khurana,[1] Y. J. Ma,[1] W. Kurth,[2] and T. I. Gombosi[3]

[1]   The major momentum-loading source in Saturn's magnetosphere, Enceladus, has been studied with seven Cassini flybys between 2005 and 2008. In this paper, we first use parameter tests with our 3-D magnetohydrodynamic simulation to demonstrate and determine the sensitivity of the interaction to both electron impact rates and charge-exchange rates. We also investigate the reasons behind our previous discovery that in the plume, within about two Enceladus radii of the plume's source, the momentum-loading rates per unit ion and neutral density are orders of magnitude lower than at greater distances. We find that depletion of hot electrons and variations in charge-exchange rates are two possible explanations for such a reduction of the momentum-loading rates. Assisted by the Cassini observations, we use our understanding of the plasma interaction to determine the temporal variation of Enceladus' neutral plume, which is important in understanding its origin, as well as the geological evolution of this icy moon. We base our study on magnetometer observations during all seven flybys to present the first comparative analysis to all flybys in 2005 and 2008. It is found that the maximum variation in gas production rates is one third the largest rate. The plasma momentum-loading rate ranges from 0.8 to 1.9 kg/s, which is consistent with previous studies.

1.   Introduction

[2]   Fed by mass and momentum picked up from its moons, the plasma disk around Saturn controls the configuration and dynamics of its magnetosphere. Understanding the mass pickup processes from these moons is an important but challenging topic. The Cassini-Huygens mission has assembled a wealth of measurements of the moons, particles and magnetic field.

[3]   While the formation and evolution of the Enceladus plume is still not fully understood from current observations, determining the time variation of the outgassing rate would help to improve our understanding of the plume evolution. Until 2008, seven Enceladus flybys were available, with good coverage of the upstream side and in the plume, as shown in Figure 1. However, the plasma interaction and its effects on the magnetic field are 3-D problems, with variations between flybys caused by several parameters, such as chemical reaction rates, background plasma conditions and temporal/spatial variations of the plume. Numerical 3-D modeling tools with measured upstream plasma densities

are required to deduce the integrated effect from the magnetic field signals observed along these 1-D paths.

[4]   By analyzing the onboard magnetometer data, *Dougherty et al.* [2004, 2006] presented the Cassini observations along the first three encounters in 2005, which contributed to the discovery of the Enceladus plume. Using the Biot-Savart method to generate field perturbations that agree with the observation, *Khurana et al.* [2007] found that the ion pickup rates within 5 R_E from Enceladus were below 3 kg/s, where R_E = 252 km is the Enceladus radius. (In earlier papers, these passes were called E03, E04 and E11 but here we use the now more commonly used names E0, E1 and E2.) *Saur et al.* [2008] then presented their estimation of the gas production rate by comparing the field perturbation with a two-fluid plasma simulation, claiming that both the gas production rate and the momentum-loading rate during E0 is about an order of magnitude larger than that of E1 and E2. With a 3-D hybrid model, *Kriegel et al.* [2009] identified downstream and anti-Saturnward tilting of the plume during E1 and E2. However, these two studies used the same upstream density for the first three flybys, while the measured upstream density varies by a factor of two. These variations may significantly affect the field perturbations as well [*Neubauer*, 1998].

[5]   In 2008, Cassini revisited Enceladus, making four close encounters (E3, E4, E5 and E6), penetrating into the plume with the closest approach (CA) altitudes several times lower than the 2005 flybys. In addition, the CA locations of

[1]IGPP, University of California, Los Angeles, California, USA.
[2]Department of Physics and Astronomy, University of Iowa, Iowa City, Iowa, USA.
[3]Department of Atmospheric, Oceanic and Space Sciences, University of Michigan, Ann Arbor, Michigan, USA.
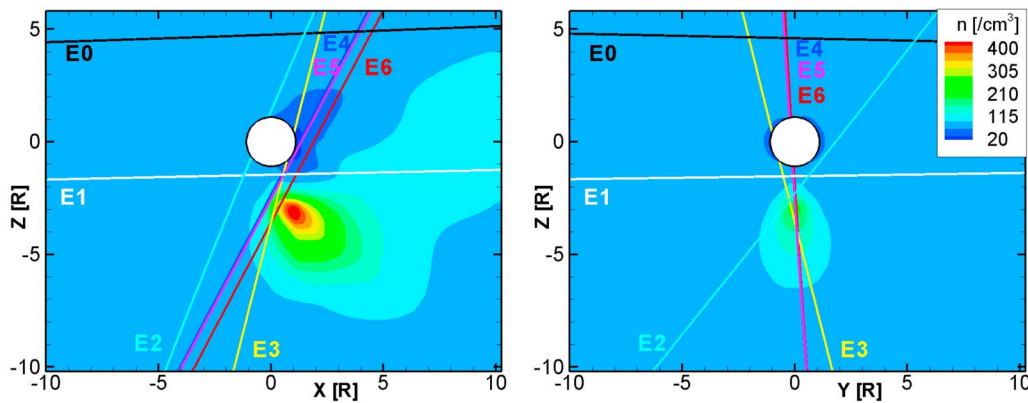
Figure 1. Cassini trajectory of the seven flybys studied in this work. Shown are projections in the $y = 0$ and $x = 0$ planes. Background plasma number density contours are extracted from a representative model result (the best fit case to E5) to mark the pileup location.

the 2008 flybys clustered on the downstream side of the moon, whereas all three of the 2005 flybys were on the upstream side. *Jia et al.* [2010a] presented the Cassini magnetometer observations along the 2008 flybys. Significant variations in the field perturbations were observed. Although differences in the trajectory geometry are the primary reason for differences in what the magnetometer has seen, the $|B|$ perturbations observed along two similar paths (E4 and E5) also differed by a factor of two, suggesting temporal variations in the plasma pickup rate between August and October of 2008.

[6] This paper presents the third step of our study which uses a combination of magnetohydrodynamic (MHD) simulations and these measurements to obtain an understanding of the underlying processes. In the first step we modeled the general interaction between the plasma disk and the icy moons [*Jia et al.*, 2010b]. The study not only provides comparable results to enrich the studies using magnetometer observations [*Khurana et al.*, 2008] and hybrid simulations [*Roussos et al.*, 2008] on these dielectric moons, but also presents interactions between a sub-magnetosonic flow and a momentum-loading region. Among these saturnian moons, Enceladus is the primary provider of water group ions to the magnetodisk, through its plume centered on the south pole. The Enceladus plume is composed of multiple jets [*Spitale and Porco*, 2007], but in this study we focus on the moon-scale dynamic structures, thus a single plume is used to approximate the neutral distribution. The B_z component is used for the estimation of the gas production rate, which calculates the cumulative effect of all momentum loading along the streamlines, so the fine structure of the plume should not cause any significant differences to our result.

[7] For the second step, we modeled the interaction between the plasma disk and Enceladus with its neutral plume [*Jia et al.*, 2010c]. By comparing our 3-D MHD simulation results with the magnetometer observations of such an interaction region along two Cassini flybys, one in 2005 and one in 2008, a collection of parametric studies were presented. These comparisons illustrated the effects of the gas production rate, chemical reaction rates (charge exchange, photo ionization, and electron impact ionization), upstream conditions and shape of the plume on the field perturbation. In both paper 1 and paper 2, it was also shown that the magnetized disk plasma is primarily affected via momentum loading associated with charge exchange, instead of mass loading caused by photoionization, as is important on active comets. For comparison, in the Jovian magnetosphere, the momentum-loading rate is only a few times larger than the mass loading rate of the (sulfur and oxygen) plasma source, from Io and Europa [*Combi et al.*, 1998; *Kabin et al.*, 1999].

[8] In this third modeling paper, we apply the code presented in papers 1 and 2 to each of the seven flybys from 2005 to 2008. In section 2, we review our model and method. In section 3, we discuss the effects of chemical reactions to stress the feasibility of our method. Section 4 presents the model results compared with the magnitude of the field, constraining the time variation of the plume. Section 5 summarizes the study.

2. Model Description

[9] In this paper we exercise the same Block Adaptive Tree Solar wind Roe Upwind Scheme (BATS-R-US) [*Tóth et al.*, 2005] code used in papers 1 and 2 with the same set of parameters, with the following exceptions: For cases in section 3, the adjusted chemical reaction rates are listed in Table 1; while in section 4 the gas production rates and upstream plasma density are listed in Table 2.

Table 1. Summary of Simulation Cases

Case	f_i (10^{-8} s^{-1})	k_{in} (10^{-15} m^3 s^{-1})	u_∞ (km/s)	Neutral Plume Density
Best Fit	2	2	26	n'_{np}
1	4	2	26	n'_{np}
2	2	4	26	n'_{np}
3	2	2	16	n'_{np}
4	2	2	26	n_{np}
5	equation (3)	2	26	n_{np}
6	2	equation (5)	26	n_{np}

Table 2. Time Variation of the Plume Gas Production and Momentum-Loading Rate[a]

	Flyby						
	E0[b]	E1	E2	E3	E4	E5	E6
Year	2005	2005	2005	2008	2008	2008	2008
Month/Day	02/17	03/09	07/14	03/12	08/11	10/09	10/31
Closest Approach (R_E)	6.0	3.0	1.7	1.2	1.2	1.1	1.8
Upstream density n_∞ (cm^{-3})	90	70	70	90	55	90	45
Q_p (10^{28} s^{-1})	3.2	2.2	2.8	3.2	2.4	2.6	2.6
Q_p (kg s^{-1})	900	600	800	900	680	740	740
Momentum-loading rate (kg/s)	1.9	0.8	1.3	1.9	0.8	1.3	0.9

[a]For flybys E0, E1 and E2, the density is calculated from its SKR longitude system [*Kurth et al.*, 2007]. The longitudes in the SLS 2 system (named by *Kurth et al.* [2008]) of these three flybys are 331, 61, 220 degrees, respectively. For the other flybys, the density was determined by Cassini RPWS's electron density measurement. The closest approach distance is measured from Cassini to the moon center.
[b]The agreement for E0 is judged with a different criterion.

[10] To simulate the plasma environment around Enceladus we consider the interaction of the magnetospheric field and plasma with the Enceladus surface and gas plume. As in our previous papers, we center our coordinate system at Enceladus, with the x axis pointing along the corotating flow, y axis toward Saturn, and z axis pointing up to complete the right-handed system. We call these coordinates the ENIS system [*Dougherty et al.*, 2006]. We solve the 3-D MHD equations by treating the plasma-neutral reactions as source terms to the mass, momentum and energy flux.

[11] Our simulation domain is a cube of $80 \times 80 \times 80 R_E$. A multiscale grid system is used, with the smallest grid size (10 km) located at the surface and in the plume. Enceladus is treated as the inner boundary so that we do not simulate the region below its surface. The plasma is absorbed at the Enceladus surface, while the magnetic field has zero gradient across the boundary. The upstream boundary of the calculation domain uses an inflow condition, in which all parameters are kept constant (see Table 2 of paper 1 unless specified). The field and plasma conditions are fixed at the y and z boundaries as well. At the downstream boundary, a float condition is used, where the information passes out of the calculation domain along the streamlines. A dipolar magnetic field is used as the background. The difference between an ideal dipole and the observed background field is about 10 nT, which is mostly due to the northward shift of Saturn's dipole. Such a shift along the dipole axis does not create differences for different longitudinal locations of Enceladus. Cassini observations show that the difference between flybys are less than 2 nT, which is due to exterior sources (the CAM). Our test shows that the model result is not sensitive to such global-scale variations in the background field, so the difference is compensated by uniform field values ranged within 10 nT.

[12] The neutral plume is treated as a background condition. The plume structure and density are not affected by reactions with the plasma. To study the effects of variable reaction rates, the neutral density and reaction rates used are described in section 3 and Table 1, meaning that in the outcome of the interaction, any variability would depend on both the different upstream conditions and gas production rates of each scenario. To study the plume variation we use the same neutral density function n'_{np} as in previous studies [*Jia et al.*, 2010c]:

$$n_{np} = \frac{Q_p}{A u_n r_p^2} e^{\left(-(\theta/\theta_H)^2 \ln 2\right)} \tag{1}$$

$$n'_{np} = \begin{cases} n_{np} \times e^{\left(-\alpha(R_{p0}-r_p)\right)}, & r_p \leq R_{p0} \\ n_{np}, & r_p > R_{p0} \end{cases} \tag{2}$$

In equations (1) and (2), Q_p is the gas production rate that is given in Table 2; θ_H defines the width of the plume; $r_p = \sqrt{x^2 + y^2 + (z + 1 R_E)^2}$ is the distance to the south pole; $u_n = 0.3$ km/s is the neutral velocity; and $A = 0.536355$ is an integration constant when $\theta_H = 20°$ [*Jia et al.*, 2008]. The normalized distance R_{p0} equals 1.8 and defines the region in which ion-neutral reactions are reduced. Alpha is 3.0 and determines the rate at which the neutral density is reduced. These values are determined empirically. In equations (1) and (2), θ is the location angle from the south pole relative to the plume axis. The plume axis is tilted by θ_T in the $x - z$ plane from the $-z$ axis.

[13] In their studies, *Saur et al.* [2008] and *Kriegel et al.* [2009] found variations in the plume parameter θ_T during the first three flybys by modeling the magnetometer data. We have found that both the orientation and width of the plume may affect the agreement with the magnetometer observations. In this study, that is targeted on an estimation of the relative variation of the production rate, we leave these parameters fixed ($\theta_H = 20°$, $\theta_T = 10°$) and only vary the production rate Q to achieve the best fit.

[14] In our previous study we used 70 cm^{-3} as the upstream plasma density and showed the effect of its variations. In practice the plasma density upstream of Enceladus varies with time [*Gurnett et al.*, 2007]. In section 4 the upstream density is determined from two sources. For the 2005 flybys, it is determined by the averaged value from the Cassini survey at Saturn's plasma disk [*Gurnett et al.*, 2007, Figure 2]. We calculate the Saturn kilometric radiation (SKR) longitude of each of the 2005 flybys from the equations by *Kurth et al.* [2007]. For the 2008 flybys such a coordinate system is not available so we use the upstream electron density measured by the Cassini Radio and Plasma Wave Science (RPWS) from waves at the upper hybrid frequency. The values of the density are listed in Table 2.

3. Effect of Various Parameters

[15] It is believed that charge exchange is the dominant reaction that slows down the plasma at the plume center [*Burger et al.*, 2007]. By comparing our interaction model, that considers only charge exchange, with a model that has only photo and electron impact ionization, it was shown that the photoionization and impact ionization processes significantly increase the plasma density at the plume center. The newly created ions are immediately picked up by the ambient plasma and then react with the plume neutrals to provide additional charge exchange that is comparable to the amount of charge exchange between the upstream disk ions and plume neutrals. Thus photo and electron impact ioni-
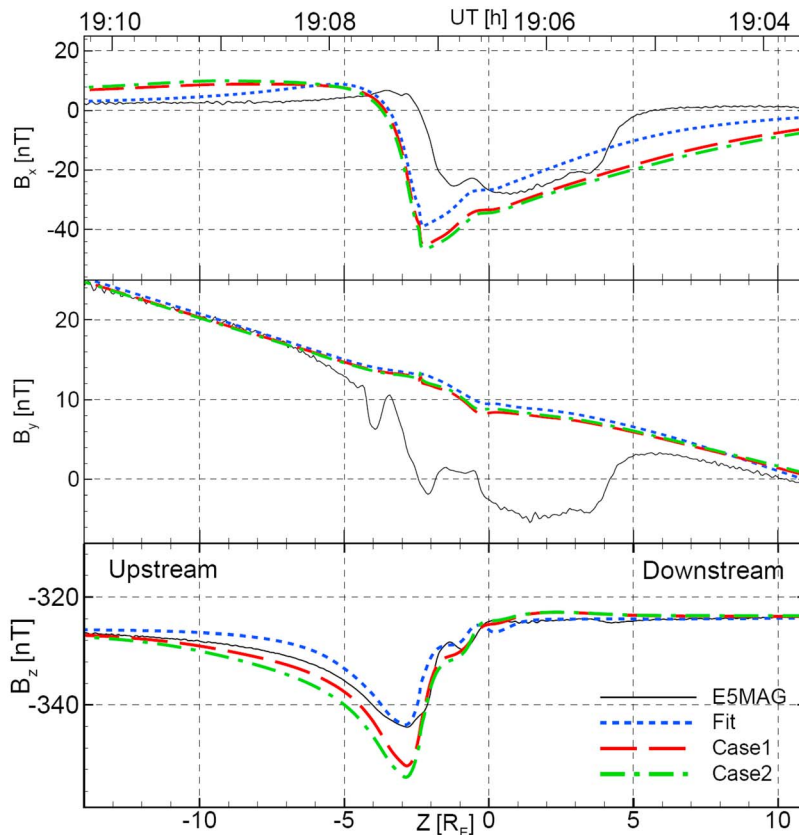
JIA ET AL.: VARIABILITY OF ENCELADUS PLUME

Figure 2. Effect of increased impact ionization rate (case 1) and charge-exchange rate (case 2) shown with the three components of the magnetic field along the Cassini E5 trajectory. The blue dotted lines show the result with the best agreement.

zations provide a significant ion source for extra charge exchange, which is equally as important as the charge exchange between torus ions and plume neutrals in controlling the slowing down of the plasma [*Jia et al.*, 2010b, 2010c]. In this section we quantify the effects of variable electron impact ionization rates and charge-exchange rates. The E5 flyby is chosen for model data comparison to maintain consistency with our previous studies.

3.1. Effect of Variation in Chemical Reaction Rates

[16] Cassini has found that the undisturbed electron temperature near Enceladus is close to 1 eV. The electron impact ionization is powered by the relatively warm (13 eV, or 1000 km/s) component of the electrons [*Tokar et al.*, 2006; *Burger et al.*, 2007]. Currently there is no accurate measurement of the density of these warm electrons for each of the flybys, so we use our parameter study compared with measurements along the E5 trajectory to show the effects of various populations of warm electrons. In case 1 we uniformly double the total of photo and electron impact ionization rate constants, while the result is shown as red dashed lines in Figure 2. The black lines represent the magnetometer measurement along the E5 flyby, while the blue lines denote the best fit case shown in paper 2.

[17] In previous studies, it is established that the Enceladus plume acts as an obstacle to the upstream flow, and thus bends field lines around its center. To the north of the plume center, the B_x perturbation is negative, while to the

south, B_x is positive. The B_y perturbation is octupolar. At negative y above the obstacle, B_y is negative at upstream and positive at downstream. The signs reverse at positive y above the obstacle, or at negative y below the obstacle [*Jia et al.*, 2010b, Figures 3a, 4a, 5a, and 6b]. At the upstream side of the obstacle, B_z increases, while at the downstream side, B_z decreases. However, the signs of these field perturbations (especially B_y and B_z) observed by Cassini are not consistent with predictions using an obstacle centered either at Enceladus or at the south pole of Enceladus. As the number of investigations and observations increases, these disagreements remain. Our study matches the B_z component while deferring the matching of the B_y signatures to future global models through the consideration of the Enceladus interaction within its larger neutral torus and enhanced by its orbital resonance with the circulation of the magnetospheric plasma (C. T. Russell et al., manuscript in preparation, 2010).

[18] As illustrated in Figure 1, the closest approach of E0 lies to the north and upstream of the obstacle, while that of E1 lies to the south and upstream of the obstacle. E2 went from south to north at the upstream side, while the 2008 flybys have comparable trajectories that penetrate the plume center. Increasing the rate of chemical reactions effectively increases the rates of plasma pickup, and thus increases the intensity and range of the perturbation, which is expected to be seen along E5.

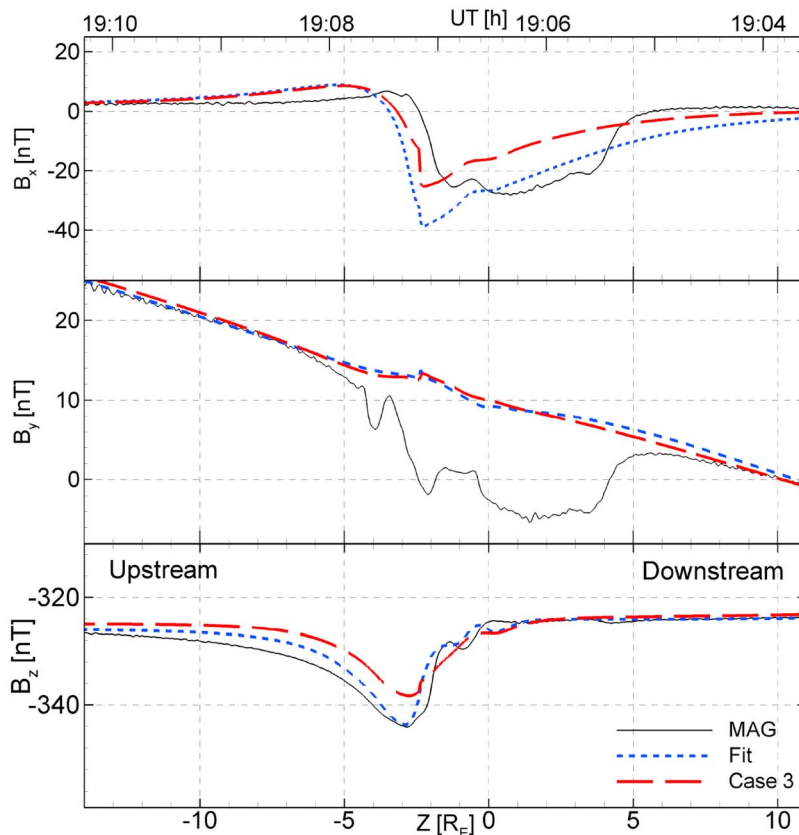[19] Compared with the best fit case, the case 1 result shows a 40% increase in the maximum |B| perturbation. The

Figure 3. Effect of low upstream velocity (case 3) shown with the three components of the magnetic field along the Cassini E5 trajectory. The blue dotted lines show the best fit result.

magnitude of the B_x perturbation is 15% larger on the downstream side, while it is similar on the upstream side. The extent along the z axis in which the B_x perturbation is above 2 nT is about twice that of the best fit case, indicating a larger region of flow deceleration. The differences of the B_y perturbations from these results are less than 2 nT.

[20] The charge-exchange reactions occur at different rates for different water species. The maximum value of the charge-exchange rate is estimated to be 4×10^{-15} m^3 s^{-1} with a relative speed above 26 km/s [*Burger et al.*, 2007], which is twice the value used in our nominal cases. In case 2, we use 4×10^{-15} m^3 s^{-1} to estimate the upper limit of charge-exchange reactions, which is shown with the green dashed-dotted lines in Figure 2. The magnitude of the B_x perturbations in the case 2 result is less than 5% different from the case 1 result, which is about 15% larger than the best fit. The magnitude of the B_y perturbation is similar to the case 1 and best fit results. The magnitude of the B_z perturbation in the case 2 result is 5% larger than the case 1 result, which is also 40% larger than the best fit result. Since the B_z component is an order of magnitude larger than the other two components, $abs(|B| - |B_z|)/|B|$ is less than 0.5% in the entire interaction region.

[21] In general, doubling the total of photo ionization and electron impact ionization rates or doubling the charge-exchange rate causes a similar increase in the momentum loading rate and thus in the perturbation to $|B|$. Such increases cause a limited increase in the B_x and B_y components, although the extent along the z axis that is substantially disturbed is significantly increased: The B_x perturbation doubles its extension to the downstream and north side of the plume, while the B_z perturbation doubles its extension to the upstream side of the plume. Along E2 and the rest of 2008 flybys, the results are the same because of their similar geometry. Along E1, the extensions where B_x and B_z are disturbed are not significantly changed, while the extent of B_y perturbations increases toward the downstream side by less than half. Overall, the parameter study of reaction rates justifies the use of $|B|$ in section 4 below to probe the relative variation in gas production rates, even before we fully model the global circulation along the Enceladus orbit which we deem necessary to explain the B_x and B_y observations.

3.2. Effect of Variation in Upstream Flow Speed

[22] In our studies, the upstream plasma velocity has been assumed to be the corotation velocity of 40 km/s. However, *Wilson et al.* [2009] looked into the Cassini Plasma Spectrometer (CAPS) observations during 2005 and 2007 at the Enceladus orbit when Enceladus itself was far away from the spacecraft, and identified 75% subcorotation in the plasma disk flow speed. Such a lower upstream momentum should result in lower momentum-loading rates. In this section we quantify the effect of such a variation by analyzing the magnetic perturbations along the E5 trajectory.

[23] In case 3 we keep other parameters at nominal values while changing the upstream velocity to 16 km/s. The new relative velocity between the plasma and Enceladus (with its

orbital speed 12.6 km/s) approximates the observed subcorotation speed (about 75% of 40 km/s). The resulting field perturbation along E5 is shown in three components in Figure 3. The perturbation to the B_y component is less than 2 nT so the difference between these two simulation runs is not as obvious as their respective differences from the observation, which is interpreted by a deflection of the flow in the radial direction of Saturn which we did not include here. Because the difference between the best fit case and case 3 is in the upstream momentum, the difference between the two model results is observable in B_x and B_z, while the shape of the perturbation remains the same. The Alfven speed is about 10 times larger than the flow speed so the variation in Alfven wing angle (arctan(M_A)) caused by the variation in upstream flow speed is only a few degrees. Both components in the case 3 result show 35% less perturbation in magnitude than the best fit case. The field perturbation exhibits an approximately linear dependence on the upstream velocity. Consequently, for such a 75% subcorotating flow, the production rate that is required to model the observed field perturbations should be around 30% higher than what we are using in our best fit cases.

3.3. Effect of Depletable Hot Electrons

[24] The primary ionizing electrons are those with an energy of 13 eV or more. These warm electrons lose over 10 eV of energy once they collide and ionize a water molecule, reducing the probability of further ionization of other molecules by over 2 orders of magnitude [Rao et al., 1995; Itikawa, 2005]. These warm electrons travel with thermal velocities along the field over 10 times faster than the corotational speed across the field. Thus other than the absorbing moon surface, only the regions with highest neutral density or dust density may deplete these electrons. The neutral density at the plume center ranges between 10^{15} to 10^{16} m^{-3} in our model, which is consistent with the Cassini UVIS and INMS observations [Hansen et al., 2006; Cravens et al., 2009]. At this density, a warm electron with 1×10^{-22} m^2 reaction cross section [Rao et al., 1995] has a mean-free path of 1000 to 100 km, which is comparable to, or smaller than, the scale of the plume. In addition, recent observations suggest that the electron density may be significantly depleted in the plume from negative charging of the dust particles [Farrell et al., 2009; Jones et al., 2009; Coates et al., 2010].

[25] Another reason to study the effect of reaction rates is to reach the same effect of the phenomenological reduction of the neutral density at the plume center. Theoretically, a typical obstacle in a magnetized flow results in pile up in front of the obstacle and rarefaction at the downstream side [Sonett and Colburn, 1968, Figure 14]. In the Enceladus case, such a standard model results in an upstream increase/downstream decrease in $|B_z|$ and B. The Cassini 2005 flybys went through the upstream side and observed the $|B_z|$ increase. The Cassini 2008 flybys penetrated the plume from the downstream side. The magnetic field measurements along these 2008 paths show a nearly 10% increase but no decrease in $|B_z|$. We interpret the lack of $|B_z|$ decrease as a geometry effect: Using an empirical function (equation (2)) to reduce the neutral density in the plume center, the momentum loading center is shifted about 2 R$_E$ in the $-z$ direction, and thus the trajectories originally de-

signed to penetrate the region of $|B_z|$ decrease is now above this region [Jia et al., 2010c].

[26] In this paper we investigate why a decreased neutral density may reproduce the magnetometer observation by altering the chemical reaction rates. In cases 5 and 6 we show parametric studies to quantify the effects of these variable rates, while the self-consistent solution of such chemical reactions close to the plume center requires the multispecies code in our next stage of this series of study. On the other hand, although charged dust may be locally affecting the field close to this region as well, we also leave such study to future studies with multifluid codes because the variations in chemical reaction rates partly account for the downshift of the momentum-loading center.

[27] In cases 4, 5 and 6, we use n_{np} from equation (1) for the neutral density in the plume. The only difference between case 4 and the best fit case is the neutral density function; thus case 4 is identical to case 1 in our paper 2, and is presented for comparison in this work.

[28] The blue dotted lines in Figure 4 represent the case 4 result in all three components along E5. The black solid lines show the magnetometer measurements. In contrast to the best fit case shown in Figure 2, both the B_x and B_y components of the case 4 result exhibit significant bipolar disturbances when $-3 < z < -1$ R$_E$. In addition, the modeled field magnitude $|B|$ along E5 shows a significant decrease close to and downstream of the moon's surface, as expected from a simple momentum-loading obstacle to the flow.

[29] In case 5, the electron impact ionization rate f_{imp} drops to zero when the neutral density is above 10^{15} m^{-3}:

$$f_{imp} = \begin{cases} f_{imp\infty}, & n_n \leq 10^{15}\,\text{m}^{-3}, \\ 0, & n_n > 10^{15}\,\text{m}^{-3}, \end{cases} \tag{3}$$

where $f_{imp\infty} = 1.6 \times 10^{-8}$ s^{-1} is the electron impact ionization rate, which is added to the photoionization rate f_{ph} to achieve the total electron-creating ionization rate f_i. The neutral density n_n is the sum of the plume component n_{np} and the negligible spherically symmetric component [Jia et al., 2010c].

[30] The red dashed lines in Figure 4 show the effect of such variations in the electron impact ionization rate. For the B_x component, the case 5 result reproduces the data within $-3.5 < z < -2$ R$_E$, while the case 4 result does not. In 3-D, this difference indicates that the center of momentum loading in the case 5 result is 1 to 2 R$_E$ lower than in the case 4 result. Figure 5 compares cases 4 and 5 in 2-D cuts. In Figures 5a and 5d, the momentum loading center can be seen 1–2 R$_E$ lower in the case 5 result (color maps) than in the case 4 result (blue contour lines). The difference between the two case results are not obvious in the z = 0 plane because it is to the north of the momentum-loading center. However, the differences between the two case results are obvious in the plane cut along the trajectory. This plane is parallel to the y axis. The B_x difference along E5 between $-3.5 < z < -2$ R$_E$ in Figure 4 is also seen in Figure 5c: Two more contour levels are seen in the case 4 result but not in the case 5 result. The reason is shown in Figure 5a: As the momentum-loading center moves up, Cassini encounters a stronger positive B_x.
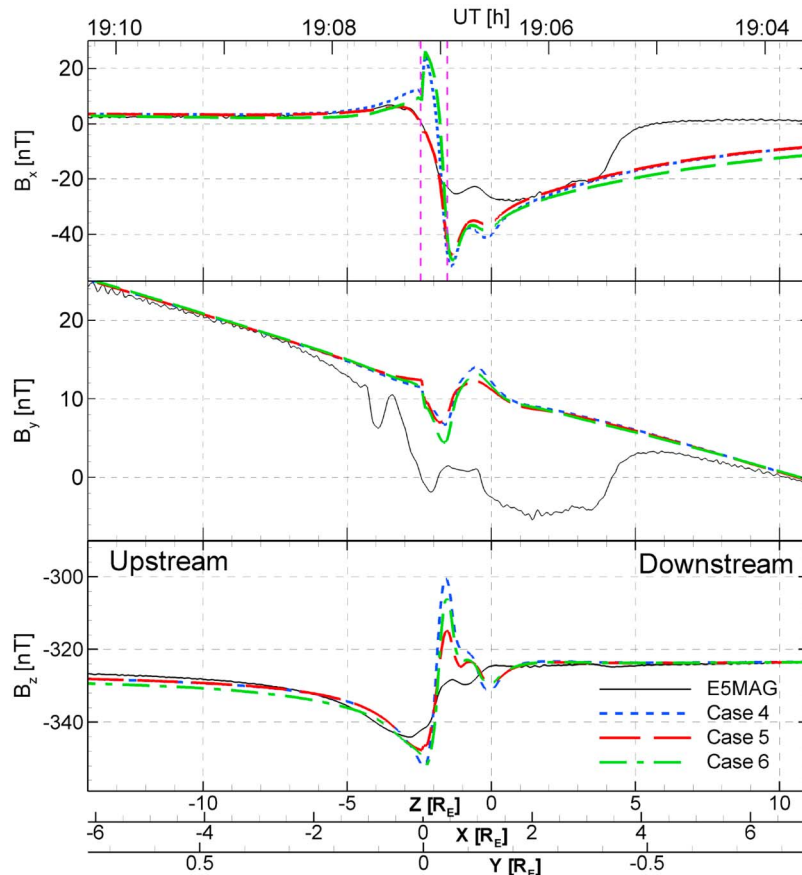
Figure 4. Effect of variable electron impact ionization rate (case 5) and charge-exchange rate (case 6) shown with the three components of the magnetic field along the Cassini E5 trajectory. Case 4 in the blue dotted line is the case 1 result in paper 2 added for comparison. The pink vertical lines in the B_x plots mark the outer boundaries of the region where the neutral density exceeds 10^{15} m^{-3} in the model.

[31] In summary, During E5, Cassini passed both above and below the center of momentum loading in the case 4 result, while it only passed above this center in both the best fit case and case 5 result. The depletion of impact electrons results in a lower ion pickup rate in the plume within 2 R$_E$ from the south pole, which is responsible for moving the momentum-loading center southward.

[32] A similar test case with half the gas production rate does not reproduce the B_x perturbation in this segment because it does not provide sufficient momentum loading (it results in less perturbation to |B| than observed). In other regions, the case 5 result for B_x is similar to the case 4 result. For the B_y component, the perturbation in the case 5 result is less than half that of the case 4 result at $-1 < z < 0$ R$_E$. For the B_z component, the case 5 result shows 10% less maximum increase in magnitude and 60% less maximum decrease than the case 4 result. These effects are visible along all 2008 paths but along none of the 2005 paths, because the 2005 paths are primarily upstream. Although the magnetometer data are not completely reproduced with this simplified electron impact ionization profile, the improvement from the case 4 result encourages us to include variable impact ionization rates in future studies to improve the accuracy.

3.4. Effect of Velocity-Dependent Charge-Exchange Rate

[33] The water molecules ejected from Enceladus dissociate to create H, O and OH neutral particles in the neutral torus. These neutrals are ionized into H$^+$, O$^+$, OH$^+$, H$_2$O$^+$ and H$_3$O$^+$ ions. Throughout the interaction region around Enceladus, although these particles dominate the neutral and ion species, and can be grouped into Hydrogen and water group particles, the cross sections for charge exchange may vary by a factor of 3 between different ion species. In addition, the relative velocity between ions and neutrals varies from less than 5 km/s to 26 km/s in our model, while these cross sections are different at these relative velocities. In their study of the chemical reactions in the water plume of Enceladus, [*Burger et al.*, 2007] summarized the cross sections between these water group ions and neutrals at two different velocities.

[34] With our current single-species code, we combine these reaction cross sections by assuming a constant number density ratio (1:1) between all five of the ion species. With such an assumption the averaged charge-exchange rates (k_{in}) between ions and neutrals can be estimated from their charge-exchange cross sections [*Lishawa et al.*, 1990] as: 4×10^{-15} m^3 s^{-1}, 3×10^{-15} m^3 s^{-1} and 2×10^{-15} m^3 s^{-1}
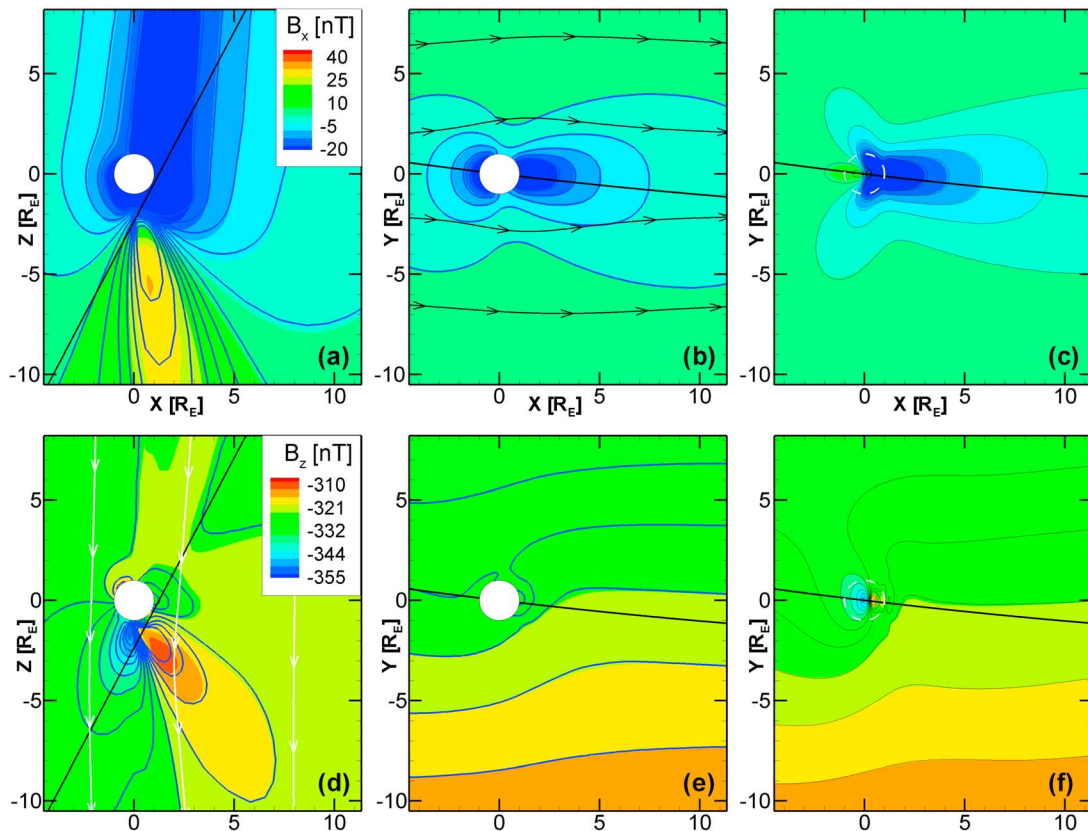
Figure 5. Magnetic field contours of cases 4 (as blue lines) and 5 (as color map). (top) The B_x contours, (bottom) B_z contours. Shown are (a and d) $y = 0$ slices, (b and e) $z = 0$ slices, and (c and f) 2-D slices along the E5 trajectory, which is marked by the straight black line. Black and white arrowed lines show the streamlines and field lines, respectively.

at velocities of 26 km/s, 15 km/s, and 1 km/s, respectively. When the relative velocity between ions and neutrals is low (<2 eV, or 3 km/s), H_3O^+ becomes dominant [*Cravens et al.*, 2009] and thus only elastic collisions between H_3O^+ and neutrals are left. In this region the elastic collision rate can be calculated using equation (4) [*Banks and Kockarts*, 1973; *Backes*, 2004]:

$$\nu_{in} = 2.6 \times 10^{-15} \sqrt{\frac{\alpha_0}{\mu_{in}}} m^3/s \approx 1.06 \times 10^{-15} m^3/s, \quad (4)$$

where the polarizability, α_0, for the nonresonant collision is 1.5 in units of 10^{-24} cm^3, according to [*Schunk and Nagy*, 2000], and $\mu_{in} \approx 9$ is the reduced mass of ions and neutrals.

[35] In case 6, we combine the estimations above and approximate the reaction rate with a step function as determined by the relative velocity:

$$k_{in} = \begin{cases} 4 \times 10^{-15} m^3 s^{-1}, & u \geq 20 \, km/s \\ 3 \times 10^{-15} m^3 s^{-1}, & 20 > u \geq 10 \, km/s \\ 2 \times 10^{-15} m^3 s^{-1}, & 10 > u \geq 3 \, km/s \\ 1 \times 10^{-15} m^3 s^{-1}, & u, 3 \, km/s \end{cases}, \quad (5)$$

where u is the plasma bulk velocity, which is at least several times larger than the neutral velocity $u_n = 0.3$ km/s. Because

in most regions $u \approx u_x$, The spatial distribution profile of u and its value along E5 can be approximated from the u_x values plotted by *Jia et al.* [2010c, Figures 2 and 6], respectively.

[36] The green dashed-dotted lines in Figure 4 show the case 6 result. Due to the doubled charge-exchange rate at larger distances, a slightly larger amplitude of perturbation can be seen when $z > 3$ R$_E$ in B_x and $z < -3$ R$_E$ in B_z. The magnitude of the perturbation between $z = \pm 3$ R$_E$ lies between the case 4 and case 5 results: The B_x perturbation is similar to case 4, the minimum of the B_y perturbation is even 60% smaller than those of cases 4 and 5; while the maximum of the B_y perturbation is close to the case 4 result. As a relatively low charge-exchange rate is used in this region, the pickup rate is slightly lower in case 6 than what is modeled in case 4, and the center of momentum loading is only slightly moved in the $-z$ direction. This is caused by the large Alfven speed. The deceleration of flux tubes propagate along the field lines over 10 times faster than they convect along the flow. Thus a velocity-dependent charge-exchange rate by itself is not sufficient to move the center of momentum loading 2 R$_E$ southward of the south pole.

[37] The B_z minima of cases 6 and 4 are similar, while the maximum decrease of B_z in the case 6 result is 15% less than that of the case 4 result. Based on our results shown in cases 1 and 2, this can be understood by a

variation in the charge-exchange rates from twice the original value ($k_{in} = 2 \times 10^{-15}$ m^3 s^{-1}) to half the original value.

[38] Similar to the effect of impact ionization rates, variations in charge-exchange rates do not result in any significant change in the perturbations along the 2005 paths, but the overall perturbation is stronger. This is because the rate we used for previous studies is half the rate we used for case 6 when the relative speed is close to the background flow speed. Comparable effects to the case 6 study are seen along the remainder of the 2008 paths. The differences between case 4 and case 6 are weaker along E4 and E6 because their production rates are smaller. For a subcorotating upstream flow, the charge-exchange rate is smaller in regions outside the plume. In the plume where most of the momentum loading happens, this rate is similar, although the size of the region where the flow is slow should be larger, and thus the absolute reaction rates are smaller than our current model prediction. Such variations should be considered in future models to improve the accuracy.

[39] In general, the case 5 and case 6 results do decrease the differences between the model and Cassini observations. Combining the effects of these two may move the momentum-loading center closer to what is observed by Cassini. Thus a multispecies code that treats the reaction rates more precisely is a plausible way to interpret the interaction close to the surface, and thus to self-consistently solve the neutral density problem raised in paper 2. *Fleshman et al.* [2010] pointed out the importance of variations in reaction rates with a chemistry code using a predefined flow field. Self-consistent simulations are needed to quantify the feedback of these rate variations on the plasma.

[40] The location where the B_x perturbation turns its sign is determined by the draping signature of the field, or the relative degree the flow is decelerated. In our 3-D simulation result of the best fit case, such turning points locate on a cylindrical surface along the northern Alfven wing. The bottom of the cylinder is about 3 R$_E$ from the origin. In the x direction, the cylinder is about 3 R$_E$ upstream and 5 R$_E$ downstream. In the y direction, the cylinder is less than 1.5 R$_E$ in both directions. The bottom of the cylinder is approximately parallel to the z = 0 plane. In the z direction, the bottom of the cylinder is coincident with the maximum of $|B_z|$ perturbation, the minimum of u_x the neutral density peak and the ion density peak. In the x direction, the peak of $|B_z|$ is about half R$_E$ upstream of the u_x minimum, which is coincident with the neutral and plasma density peak. The spatial variation in these reaction rates leads to the spatial variation in the locations of $B_x = 0$ or $|B_z|$ maximum.

[41] Although the 3-D shape of these locations are more irregular than those of the best fit case result, the relative z location of $B_x = 0$ and x location of $|B_z|$ maximum compared with the locations of u_x minimum and density peak remains roughly the same. Thus the vertical location (z direction) of the center can be estimated by where the B_x perturbation turns its sign, while the horizontal location (along the streamline) of the center can be estimated from where the $|B_z|$ increase is maximum. The trajectories of E3 through E6 probes through the center of the plume with north-south paths. These trajectories are ideal for the identification of the center location and strength of momentum loading, which is investigated in the next section.

4. Time Variation During the 2005 and 2008 Encounters

[42] In our previous study, it is found that the effect of variations in the upstream density on the field perturbations is nonlinear: a 43% decrease in upstream density results in a 30% decrease of the maximum B perturbation along E2 and 20% decrease along E5 [*Jia et al.*, 2010c]. With analytical solutions, *Neubauer* [1980, 1998] found the field perturbation to be proportional to the square root of upstream density. The variation of modeled B perturbations at different locations is approximately consistent with this square root dependency. In this study, to determine the plume intensity, we model each of the flybys individually to exclude the variations in the field perturbation caused by the upstream density and trajectory differences. The neutral density function used for all modeling studies in this section is defined in equation (2). Again, such a neutral density modification is an empirical approximation of reduced chemical reactions in the plume center as discussed in paper 2, and should be replaced with more sophisticated models that treat the chemistry more accurately in the future.

[43] It was also found in paper 2 that the B_x and B_y components are significantly affected by other background conditions, most probably a large-scale flow close to Enceladus initiated by the broken force balance between centrifugal and centripetal forces. Such flow conditions change the B_x and B_y signals significantly while keeping B_z similar. Since $|B_z|$ and the field magnitude are almost identical and are both sensitive to the relative momentum-loading rate across the flux tube, in this section we fashion our model to agree with the $|B|$ observations to detect the variations in the momentum-loading rate and to determine the gas production rate. However, by having field perturbations primarily in the x and y components, E0 is an exception. The agreement for E0 is judged by all three components, as shown in section 4.1.

4.1. Modeling the Three Components of the Magnetic Field Along E0

[44] On 12 February 2005, Cassini made its first targeted Enceladus flyby, the E0 flyby. As shown by *Khurana et al.* [2007, Figure 2], Cassini traveled primarily in the radial direction toward Saturn. The magnetometer observations close to Enceladus are shown with the black solid lines in Figure 6. The plotted region is primarily on the upstream side of the moon. The closest approach distance is 6 R$_E$ from the Enceladus center. During the period of time that is shown here, Cassini is 4 to 5 R$_E$ north of the Enceladus equator. For this flyby the perturbation in $|B|$ is smaller than the amplitude of ion cyclotron waves (2 nT) [*Khurana et al.*, 2007].

[45] As shown by the blue dotted lines in Figure 6, this is the only flyby for which we can reach a solid agreement with the data in all three components with our simple single species MHD interaction model that simulates the corotational flow in a straight line. The similarity between the model result and magnetometer measurements suggests that on the upstream side and above the equator, at distances
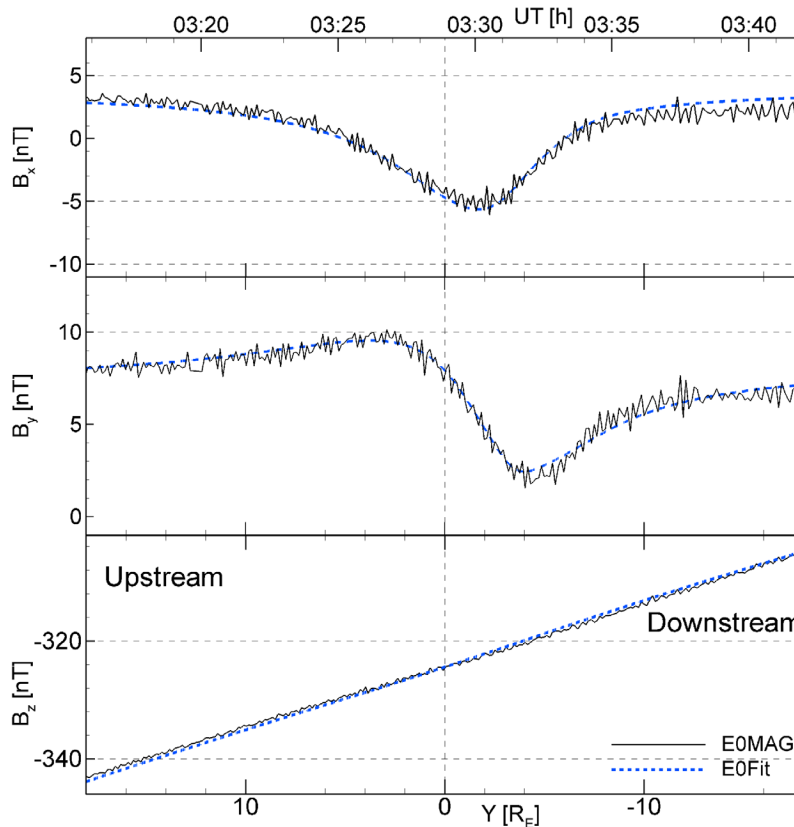
Figure 6. Model data comparison for the three components of the magnetic field along the Cassini E0 trajectory. To reveal the model result in blue dotted line, magnetometer data is shown every 6 s as the black line.

larger than 6 R_E, the field perturbation by Enceladus and its plume can be approximated by the interaction between a flow with a neutral cloud. In contrast with the other 6 flybys that prefer a "disturbed" plasma flow (such as by a flow component in Saturn's radial direction), the success in matching the signatures in the B_x and B_y components using a simple model may due to the large-scale plasma flow direction being not significantly disturbed in this upstream region. Along the E0 trajectory the detailed structure of the plume is not important.

4.2. Modeling the Field Magnitude During 2005 and 2008 Flybys

[46] The other flybys, E1 through E6, are studied using the same set of parameters except for a varying upstream density as listed in Table 2. For each flyby, the model output with different gas production rates is compared with observations until the best fit is obtained. Similar to previous studies, we calculate $\sqrt{\sum \left(B_{z,model} - B_{z,mag}\right)^2}$ within the distance where the field disturbance is above 2 nT. The subscripts "model" and "mag" represent the model results and the observations, respectively [*Jia et al.*, 2010c, section 3.3].

[47] In our tests, the gas production rates increase with a step of 0.2×10^{28} s^{-1}. Figure 7 shows our best fit to the field magnitude |B| for all six flybys. The self-variable axis uses the coordinates in which Cassini moves the fastest. For E1,

the x axis is used, while for the other flybys, the z axis is used.

[48] By comparing the production rates used between all six flybys, it is found that the minimum gas production rate is 2/3 as large as the maximum gas production rate. Such relative variations indicate that the plume production is not steady. In 2005, the production was strong during E0 in February and then weak in March, and strong again in July. In 2008, the plume was strong during E3 in March and then weaker after August. The Enceladus plume appears to consist of multiple jets that open and close. More detailed study using a more sophisticated plume model that considers the opening/closing of multiple jets [e.g., *Saur et al.*, 2008], assisted by observations using other instruments on Cassini to define the plasma density and speed, is needed to refine our knowledge of the time variation of the plume beyond this 30% variation.

[49] It should be noted that with our single species code we are not accurately converting the momentum-loading rate to a gas production rate, because we are averaging the reaction rates at different velocities. This study only determines the relative variation of the neutral plume intensity.

[50] The time variation of the plume has also been investigated by authors using other numerical methods based on the Cassini magnetometer data. With their multi-fluid code, *Saur et al.* [2008] treat the magnetic field as the background and calculate the disturbed field from the electric currents. A significant decrease in gas production
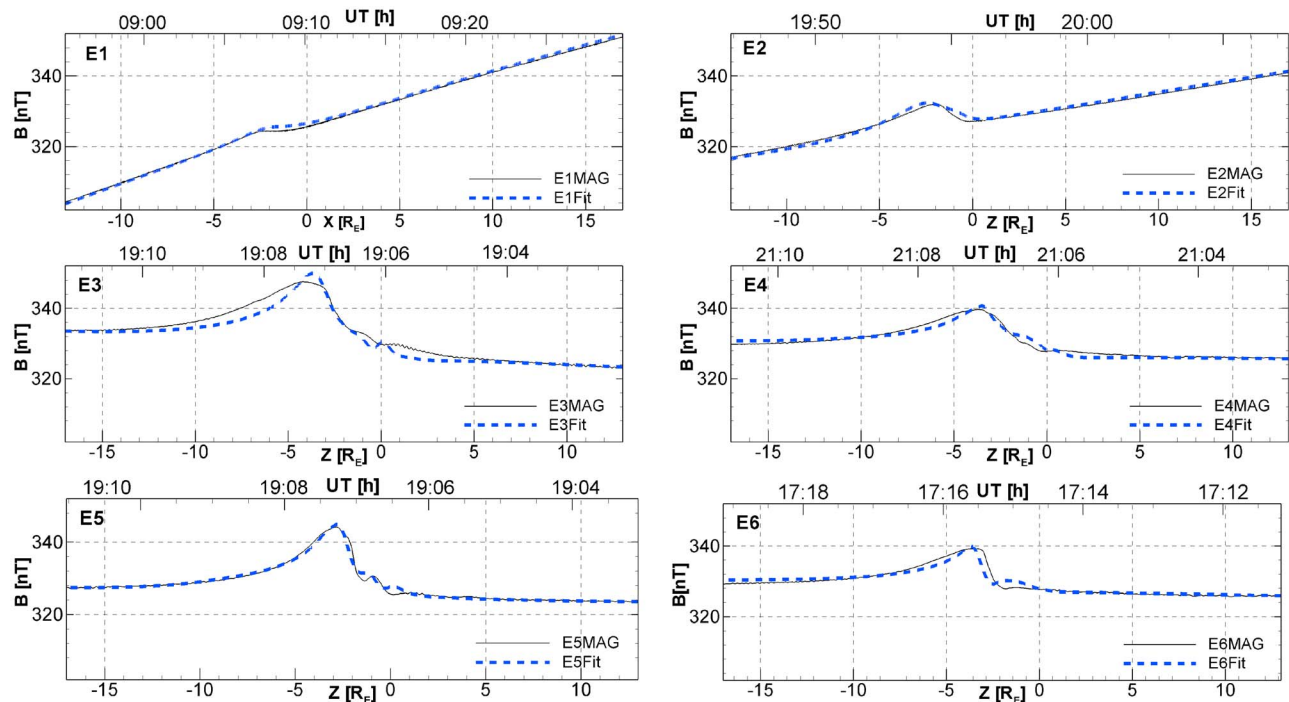
Figure 7. Best fit for the field magnitude measured during flybys E1–E6: black lines are magnetometer data; blue dotted lines are model results. All panels are organized in upstream-downstream order. E1 is plotted against the *x* coordinate, while the rest are plotted against *z*.

rate is found from E0 to E1 and E2: For an upstream ion density of 140 cm^{-3}, the production rate was found to be 5.6×10^{28} s^{-1}, while for an upstream density of 70 cm^{-3}, the production rate needs to exceed 10^{29} s^{-1}. For an upstream density of 70 cm^{-3}, the production rate was found to be 0.2×10^{28} s^{-1} during E1 and E2. In contrast, our previous study using E2 and E5 has found about 30% decrease in required gas production rate if the upstream ion density is doubled. *Kriegel et al.* [2009] modeled the magnetometer data during the E1 and E2 flybys with a hybrid code that treats the ions as particles and the assembly of electrons as a massless fluid. The gas production is decreased by half from E1 to E2, as inferred from their published momentum-loading rate. In addition, they inferred that the plume orientation has changed between E1 and E2.

[51] Once an ion is created from the neutrals via chemical reactions, it is accelerated by the motional electric field. This pickup process modifies the momentum of the ambient plasma, and thus disturbs the magnetic field. The sum of disturbances produces the total draping signature of the magnetic field, which is recorded by the Cassini magnetometer. After our simulation result reaches a steady state, we sum up the total amount of newly created ions in our 3-D data, by photoionization, electron impact ionization and charge exchange, to calculate the momentum-loading rate in each cell, and then integrate this rate over a spherical region to determine the total mass of new ions loaded into the corotating flux ropes. This sphere is centered at Enceladus with a radius of 10 R$_E$, similar to the region used by *Saur et al.* [2008].

[52] The momentum-loading rate is sensitive to the upstream plasma density, because it controls the amount of charge exchange between disk ions and plume neutrals. Thus, although the gas production rate only changes by a factor of 1.5, the momentum-loading rate varies from 0.8 to 1.9 kg/s. Again, the agreement of E0 is not judged by the same criteria, and we include its value in Table 2 for completeness.

[53] The momentum-loading rate has also been studied by various authors. The calculation by *Pontius and Hill* [2006] requires over 100 kg/s of momentum loading as inferred from the CAPS data during E2. However, the disturbed flow seen by CAPS along the E2 trajectory only points toward Saturn. We interpret this flow deflection as a Saturnward flow caused by the broken force balance between centrifugal and centripetal forces in the scale of Saturn's inner magnetosphere, instead of direct flow deflection around Enceladus [*Jia et al.*, 2010a]. *Burger et al.* [2007] has determined the momentum-loading rate to be 2 kg/s by modeling the CAPS and Ultraviolet Imaging Spectrograph (UVIS) observations. *Khurana et al.* [2007] have inverted the current system from the magnetometer observations to determine the momentum-loading rate in the range of 0.6–2.8 kg/s. The value found by *Saur et al.* [2008] is 3 kg/s during E0 and 0.2 kg/s during E1 and E2. *Kriegel et al.* [2009] have found E1 to be 1 kg/s and E2 0.5 kg/s using their hybrid model. Another hybrid model has proposed a 4 kg/s momentum-loading rate during E3 with a cosine-shaped neutral plume model [*Omidi et al.*, 2010]. Except for the estimation by *Pontius and Hill* [2006], these results are in the same range as our model results for the 2005 and 2008 flybys.

4.3. Accuracy of Our Estimations

[54] Since we are using a measurement along a single trajectory through an interacting volume, the accuracy of our production estimation is affected by a collection of parameters. Our estimation can be affected by the geometry of the trajectory. For reference, we list the distance of closest approach for each flyby in Table 2. Although we do not quantify the accuracy, the upstream flybys that are also a few times more distant should have larger error bars than the 2008 flybys. Again, the accuracy in estimating the gas production rate during E0 is limited, because the spacecraft only traveled through the distant disturbed region over 6 R_E away, upstream of the moon.

[55] We note that our study in both papers 2 and 3 is based on a simplified single-plume neutral distribution model, while the real plume may consist of multiple jets and thus the neutrals cluster in even smaller regions with an even higher density than what we use. Cassini visual images show that these jets are not always directed in the radial direction of Enceladus [*Porco et al.*, 2006]. As a result, at different altitudes, the cross section of the plume may vary. During the three 2005 flybys, *Khurana et al.* [2007] have inverted the location of the momentum-loading center from the magnetometer observations. They were inferred to be different for all three flybys. Other authors have also proposed variations in plume orientation or intensity of individual jets that form the gas plume [*Saur et al.*, 2008; *Kriegel et al.*, 2009]. In this study we keep these parameters constant to estimate the plume intensity. The uncertainty introduced by variations in the shape of the plume for the downstream (2008) flybys is of the order of our step size (0.2×10^{28} s^{-1}), while for upstream flybys it is at least twice as large.

[56] The modeled B_x and B_y components are not in solid agreement with the observation. We propose to model the large-scale flow to improve our model, which is consistent with the Saturnward motion of electron wakes distant from Enceladus [*Jones et al.*, 2006]. Such variations may cause uncertainty with the order of our step size for the 2008 flybys. We cannot quantify the size of such uncertainty for the 2005 flybys because our uniform u_y does not significantly improve our model for these flybys.

[57] In this study we vary the upstream density but keep the electron impact ionization rate the same between different flybys. It is possible that the hot electron population has changed between flybys. If the density of the hot electron population is proportional to the total electron density, the relative variation in gas production rate is expected to be smaller than listed in Table 2.

[58] The upstream flow speed in the corotational direction affects the momentum-loading rate and also the chemical reaction rates. The chemistry in the plume within 2 R_E of the south pole is not well modeled using our single-species code. It is possible that there are other dynamic processes that we did not include. These could affect the absolute value of the total gas production rate.

[59] Despite the uncertainties in these estimations of the relative production rate and the momentum-loading rate, there is no obvious relationship identified with Saturn local time or upstream plasma density. The SKR longitude calculation is not available for the 2008 flybys yet, so we do not relate the rates with SKR. In general, this study is the first step in modeling the time variation of the plume intensity using Cassini observations, and what we have found is that the intensity of the plume is not significantly different during these flybys in 2005 and 2008.

5. Discussion

[60] Enceladus is an icy moon orbiting a gas giant 10 AU away from the sun. The intense water plume at its south pole has created a unique interaction environment that involves multiple states of matter, various chemical reactions, variations in electric conductivity, and magnetic permeability with asymmetric spatial distribution that varies with time. Such a system is coupled to the saturnian magnetosphere, by tuning its plasma disk population and bending its magnetic field. We have applied quantitative physical calculations to interpret the observations, in turn revealing the complexity of this plasma laboratory.

[61] Previously we concluded that the local interaction needs to be placed in the context of the global Saturn magnetospheric circulation to address the consequences of broken force balance by the significant modification to the plasma flow speed. In this paper we show another necessary step to improving this interaction model: Both the electron impact ionization rates and charge-exchange rates decrease significantly close to the origin of the plume. Such a decrease explains why the pickup process is less efficient in this region. The magnetometer observations suggest that the center of momentum loading is about 2 R_E below the south pole. The improvement in chemistry discussed above is believed to be responsible for such a redistribution in momentum loading. Consequently, a multispecies model needs to be developed as well as a global magnetosphere code to accurately and self-consistently calculate these dynamic processes.

[62] The upstream plasma density is important in determining the gas production rate from the magnetic field perturbations. In this paper we adopt the upstream plasma density measured by Cassini RPWS to calculate the set of gas production rates during the 2005 and 2008 flybys. The maximum variation in these production rates is around 30%, while the maximum variation in the momentum loading rate is about 50%.

[63] A simple model for the plasma interaction around Enceladus would be the assembled effects of newly ionized gas particle pickup by the ambient plasma. Based mainly on the Cassini magnetometer observations and our 3-D single-species, single-plume model, we have improved our understanding of this environment in three steps. We have constrained the surface boundary condition for the saturnian icy moons, determined parameter sensitivities for the study of the Enceladus plume, and provided the relative time variation of the pickup rate and outgassing rate. In addition, we have also identified demands on future plasma-Enceladus interaction models in two major aspects: to use a global magnetodisk-Enceladus interaction model to reproduce all three components of the magnetic field measurement, and to use a multispecies model to self-consistently calculate the decreased reaction rate around the plume center.

References

Backes, H. (2004), Titan's interaction with the Saturnian magnetospheric plasma, Ph.D. thesis, Univ. zu Köln, Cologne, Germany.

Banks, P. M., and G. Kockarts (1973), *Aeronomy Part A*, Academic Press, Cambridge, U. K.

Burger, M. H., E. C. Sittler, R. E. Johnson, H. T. Smith, O. J. Tucker, and V. I. Shematovich (2007), Understanding the escape of water from Enceladus, *J. Geophys. Res.*, *112*, A06219, doi:10.1029/2006JA012086.

Coates, A. J., G. H. Jones, G. R. Lewis, A. Wellbrock, D. T. Young, F. J. Crary, R. E. Johnson, T. A. Cassidy, and T. W. Hill (2010), Negative ions in the Enceladus plume, *Icarus*, *206*, 618–622, doi:10.1016/j.icarus.2009.07.013.

Combi, M. R., K. Kabin, T. I. Gombosi, D. L. DeZeeuw, and K. G. Powell (1998), Io's plasma environment during the Galileo flyby: Global three-dimensional MHD modeling with adaptive mesh refinement, *J. Geophys. Res.*, *103*, 9071–9082, doi:10.1029/98JA00073.

Cravens, T. E., R. L. McNutt, J. H. Waite, I. P. Robertson, J. G. Luhmann, W. Kasprzak, and W. Ip (2009), Plume ionosphere of Enceladus as seen by the Cassini ion and neutral mass spectrometer, *Geophys. Res. Lett.*, *36*, L08106, doi:10.1029/2009GL037811.

Dougherty, M. K., et al. (2004), The Cassini magnetic field investigation, *Space Sci. Rev.*, *114*, 331–383, doi:10.1007/s11214-004-1432-2.

Dougherty, M. K., K. K. Khurana, F. M. Neubauer, C. T. Russell, J. Saur, J. S. Leisner, and M. E. Burton (2006), Identification of a dynamic atmosphere at Enceladus with the Cassini magnetometer, *Science*, *311*, 1406–1409, doi:10.1126/science.1120985.

Farrell, W. M., W. S. Kurth, D. A. Gurnett, R. E. Johnson, M. L. Kaiser, J. Wahlund, and J. H. Waite (2009), Electron density dropout near Enceladus in the context of water-vapor and water-ice, *Geophys. Res. Lett.*, *36*, L10203, doi:10.1029/2008GL037108.

Fleshman, B. L., P. A. Delamere, and F. Bagenal (2010), Modeling the Enceladus plume-plasma interaction, *Geophys. Res. Lett.*, *37*, L03202, doi:10.1029/2009GL041613.

Gurnett, D. A., A. M. Persoon, W. S. Kurth, J. B. Groene, T. F. Averkamp, M. K. Dougherty, and D. J. Southwood (2007), The variable rotation period of the inner region of Saturn's plasma disk, *Science*, *316*, 442–445, doi:10.1126/science.1138562.

Hansen, C. J., L. Esposito, A. I. F. Stewart, J. Colwell, A. Hendrix, W. Pryor, D. Shemansky, and R. West (2006), Enceladus' water vapor plume, *Science*, *311*, 1422–1425, doi:10.1126/science.1121254.

Itikawa, Y. (2005), Cross sections for electron collisions with water molecules, *J. Phys. Chem. Ref. Data*, *34*(1), doi:10.1063/1.1799251.

Jia, Y. D., M. R. Combi, K. C. Hansen, T. I. Gombosi, F. J. Crary, and D. T. Young (2008), A 3-D global MHD model for the effect of neutral jets during the Deep Space 1 Comet 19P/Borrelly flyby, *Icarus*, *196*, 249–257, doi:10.1016/j.icarus.2008.03.010.

Jia, Y., C. T. Russell, K. K. Khurana, J. S. Leisner, Y. J. Ma, and M. K. Dougherty (2010a), Time-varying magnetospheric environment near Enceladus as seen by the Cassini magnetometer, *Geophys. Res. Lett.*, *37*, L09203, doi:10.1029/2010GL042948.

Jia, Y., C. T. Russell, K. K. Khurana, G. Toth, J. S. Leisner, and T. I. Gombosi (2010b), Interaction of Saturn's magnetosphere and its moons: 1. Interaction between corotating plasma and standard obstacles, *J. Geophys. Res.*, *115*, A04214, doi:10.1029/2009JA014630.

Jia, Y., C. T. Russell, K. K. Khurana, Y. J. Ma, D. Najib, and T. I. Gombosi (2010c), Interaction of Saturn's magnetosphere and its moons: 2. Shape of the Enceladus plume, *J. Geophys. Res.*, *115*, A04215, doi:10.1029/2009JA014873.

Jones, G. H., E. Roussos, N. Krupp, C. Paranicas, J. Woch, A. Lagg, D. G. Mitchell, S. M. Krimigis, and M. K. Dougherty (2006), Enceladus' varying imprint on the magnetosphere of Saturn, *Science*, *311*, 1412–1415, doi:10.1126/science.1121011.

Jones, G. H., et al. (2009), Fine jet structure of electrically charged grains in Enceladus' plume, *Geophys. Res. Lett.*, *36*, L16204, doi:10.1029/2009GL038284.

Kabin, K., M. R. Combi, T. I. Gombosi, A. F. Nagy, D. L. DeZeeuw, and K. G. Powell (1999), On Europa's magnetospheric interaction: A MHD

simulation of the E4 flyby, *J. Geophys. Res.*, *104*, 19,983–19,992, doi:10.1029/1999JA900263.

Khurana, K. K., M. K. Dougherty, C. T. Russell, and J. S. Leisner (2007), Mass loading of Saturn's magnetosphere near Enceladus, *J. Geophys. Res.*, *112*, A08203, doi:10.1029/2006JA012110.

Khurana, K. K., C. T. Russell, and M. K. Dougherty (2008), Magnetic portraits of Tethys and Rhea, *Icarus*, *193*, 465–474, doi:10.1016/j.icarus.2007.08.005.

Kriegel, H., S. Simon, J. Muller, U. Motschmann, J. Saur, K.-H. Glassmeier, and M. Dougherty (2009), The plasma interaction of enceladus: 3-D hybrid simulations and comparison with cassini mag data, *Planet. Space Sci.*, *57*(14–15), 2113–2122, doi:10.1016/j.pss.2009.09.025.

Kurth, W. S., A. Lecacheux, T. F. Averkamp, J. B. Groene, and Gurnett (2007), A Saturnian longitude system based on a variable kilometric radiation period, *Geophys. Res. Lett.*, *34*, L02201, doi:10.1029/2006GL028336.

Kurth, W. S., T. F. Averkamp, D. A. Gurnett, J. B. Groene, and A. Lecacheux (2008), An update to a Saturnian longitude system based on kilometric radio emissions, *J. Geophys. Res.*, *113*, A05222, doi:10.1029/2007JA012861.

Lishawa, C. R., R. A. Dressler, J. A. Gardner, R. H. Salter, and E. Murad (1990), Cross sections and product kinetic energy analysis of H_2O^+–H_2O collisions at suprathermal energies, *J. Chem. Phys.*, *93*, 3196–3206, doi:10.1063/1.458852.

Neubauer, F. M. (1980), Nonlinear standing Alfven wave current system at Io: Theory, *J. Geophys. Res.*, *85*, 1171–1178, doi:10.1029/JA085iA03p01171.

Neubauer, F. M. (1998), The sub-Alfvenic interaction of the Galilean satellites with the Jovian magnetosphere, *J. Geophys. Res.*, *103*, 19,843–19,866, doi:10.1029/97JE03370.

Omidi, N., C. T. Russell, R. L. Tokar, and J. S. Leisner (2010), Hybrid simulations of the plasma environment around Enceladus, *J. Geophys. Res.*, *115*, A05212, doi:10.1029/2009JA014391.

Pontius, D. H., and T. W. Hill (2006), Enceladus: A significant plasma source for Saturn's magnetosphere, *J. Geophys. Res.*, *111*, A09214, doi:10.1029/2006JA011674.

Porco, C. C., et al. (2006), Cassini observes the active south pole of Enceladus, *Science*, *311*, 1393–1401, doi:10.1126/science.1123013.

Rao, M. V. V. S., I. Iga, and S. K. Srivastava (1995), Ionization cross-sections for the production of positive ions from H_2O by electron impact, *J. Geophys. Res.*, *100*, 26,421–26,425, doi:10.1029/95JE02314.

Roussos, E., et al. (2008), Plasma and fields in the wake of Rhea: 3-D hybrid simulation and comparison with Cassini data, *Ann. Geophys.*, *26*, 619–637.

Saur, J., N. Schilling, F. M. Neubauer, D. F. Strobel, S. Simon, M. K. Dougherty, C. T. Russell, and R. T. Pappalardo (2008), Evidence for temporal variability of Enceladus' gas jets: Modeling of Cassini observations, *Geophys. Res. Lett.*, *35*, L20105, doi:10.1029/2008GL035811.

Schunk, R. W., and A. F. Nagy (2000), *Ionospheres: Physics, Plasma Physics,and Chemistry*, Cambridge Univ. Press, New York.

Sonett, C. P., and D. S. Colburn (1968), The principle of solar wind induced planetary dynamos, *Phys. Earth Planet. Inter.*, *1*, 326–346, doi:10.1016/0031-9201(68)90027-7.

Spitale, J. N., and C. C. Porco (2007), Association of the jets of Enceladus with the warmest regions on its south-polar fractures, *Nature*, *449*, 695–697, doi:10.1038/nature06217.

Tokar, R. L., et al. (2006), The interaction of the atmosphere of Enceladus with Saturn's plasma, *Science*, *311*, 1409–1412, doi:10.1126/science.1121061.

Tóth, G., et al. (2005), Space Weather Modeling Framework: A new tool for the space science community, *J. Geophys. Res.*, *110*, A12226, doi:10.1029/2005JA011126.

Wilson, R. J., R. L. Tokar, and M. G. Henderson (2009), Thermal ion flow in Saturn's inner magnetosphere measured by the Cassini plasma spectrometer: A signature of the Enceladus torus?, *Geophys. Res. Lett.*, *36*, L23104, doi:10.1029/2009GL040225.

T. I. Gombosi, Department of Atmospheric, Oceanic and Space Sciences, University of Michigan, Ann Arbor, MI 48109, USA.

Y.-D. Jia, K. K. Khurana, Y. J. Ma, and C. T. Russell, IGPP, University of California, Los Angeles, CA 90095, USA. (yingdong@ucla.edu)

W. Kurth, Department of Physics and Astronomy, University of Iowa, Iowa City, IA 52242, USA.